PCCP

PAPER

View Article Online
View Journal | View Issue

Cite this: *Phys. Chem. Chem. Phys.*, 2021, **23**, 9991

The freezing behavior of aqueous *n*-alcohol nanodroplets†

Tong Sun,[a] Dor Ben-Amotz [b] and Barbara E. Wyslouzil [ac]*

Received 25th November 2020,
Accepted 14th April 2021

DOI: 10.1039/d0cp06131j

rsc.li/pccp

We generate water-rich aerosols containing 1-propanol and 1-pentanol in a supersonic nozzle to study the effects of these solutes on the freezing behavior of water. Condensation and freezing are characterized by two complementary techniques, pressure trace measurements and Fourier Transform Infrared spectroscopy. When 1-pentanol and 1-propanol are present, condensation occurs at higher temperatures because particle formation from the vapor phase is enhanced by the decrease in interfacial free energy of mixed aqueous-alcohol critical clusters relative to those of pure water. FTIR results suggest that when ~6 nm radius droplets freeze, the tetrahedral structure of the ice is well preserved up to an overall alcohol mole fraction of 0.031 for 1-propanol and 0.043 for 1-pentanol. In this concentration range, the ice nucleation temperature decreases continuously with increasing 1-propanol concentration, whereas the onset of freezing is not significantly perturbed by 1-pentanol up to a mole fraction of 0.03. Furthermore, once freezing starts the ice nucleation rates in the aqueous-alcohol droplets are very close to those for pure water. In contrast, at the highest mole fractions of either alcohol it is not clear whether droplets freeze to form crystalline ice since the final state of the particles cannot be adequately characterized with the available experimental techniques.

I. Introduction

Ice freezing from supercooled water droplets is ubiquitous in the atmosphere, and plays an important role in ice cloud formation, precipitation, and climate forcing.[1–7] Investigations of ice formation in droplets include those that characterize nucleation rates of pure water,[8–13] to those that examine the role of contaminants including inorganic materials,[14,15] biological materials,[16–18] and long-chain alcohols[19–23] resembling atmospheric oxidized organic compounds.[24–29] The variable chain-lengths of *n*-alcohols make them appealing model solutes for quantifying the influence of such amphiphilic molecules on the freezing temperature and the kinetics of ice nucleation. Here we investigate freezing in aqueous-alcohol nanodroplets formed in supersonic expansions, by combining pressure trace and FTIR measurements. Our results reveal the delicate interplay of solute size and concentration on ice-nucleation.

To date, most ice-nucleation experiments have been carried out using bulk samples or droplets that have characteristic length scales of tens of micrometers to millimeters. Thus, enrichment of the surface by amphiphilic species does not significantly change the overall composition of the sample. To our knowledge, there are no published studies reporting ice freezing of aqueous-alcohol mixtures in nanodroplets. Such studies are interesting from a fundamental point of view, because partitioning of surface active molecules in small aqueous droplets[30,31] may play an important role in determining the degree to which the presence of these species influences the freezing process of water. In particular, as the droplet curvature increases the surface/volume ratio is no longer negligible and it becomes necessary to account for the molecules lost from the bulk to the surface, *i.e.* the interior or "bulk" composition of the droplet and the surface composition both differ from the overall composition.[32] The rapid decrease in surface tension of aqueous mixtures upon the addition of alcohol, even for soluble short-chain alcohols,[33,34] and the mutual enhancement observed during vapor phase nucleation in water–alcohol systems[35,36] both confirm that surface enrichment occurs on all length scales for aqueous *n*-alcohol solutions. Furthermore, as the alcohol's chain length increases, its propensity to reside at the vapor–liquid interface increases, consistent with the lower aqueous solubility of long-chain alcohols[37] reducing the mixture surface tension more rapidly on a molar basis.[33] Consequently, other phase transition behavior, in particular freezing, may be strongly affected by the partitioning mechanism of alcohols in nanoparticles.

Previous studies have shown that short chain alcohols suppress water freezing in bulk aqueous solutions. For *n*-alcohols

[a] *William G. Lowrie Department of Chemical and Biomolecular Engineering, The Ohio State University, Columbus, OH, 43210, USA. E-mail: wyslouzil.1@osu.edu*
[b] *Department of Chemistry, Purdue University, West Lafayette, IN, 47907, USA*
[c] *Department of Chemistry and Biochemistry, The Ohio State University, Columbus, OH, 43210, USA*

† Electronic supplementary information (ESI) available. See DOI: 10.1039/d0cp06131j

containing up to four carbons, Oguni and Angell found that the $-CH_2$ groups had an additive effect on the homogeneous freezing temperature T_h depression at low alcohol concentrations.[38] A complementary study also showed that there is a linear correlation between T_h and the number of –OH groups in the alcohols and a systematic decrease in freezing temperature as the alcohol molarity increases.[39] In contrast, some aliphatic long-chain alcohols ($C > 14$) are good ice nucleators because their interfacial structure matches that of the crystal embryo of hexagonal ice, and thereby reduces the cost of forming a critical ice nucleus.[19–23]

In this paper we are interested in exploring how low concentrations of two relatively short-chain alcohols, with different alkyl chain length and aqueous miscibility, influence ice freezing behavior in nanodroplets. Note that 1-propanol is totally miscible with water near ambient temperature, whereas 1-pentanol exhibits a miscibility gap and is only soluble to a mole fraction of $x_2 \sim 0.005$. At low concentrations both of these surface-active alcohols are expected to enrich the interface of the water droplets, yielding core–shell like structures.[40,41] Much higher concentrations would be required for the aqueous-*n*-pentanol droplet to adopt the more complex phase separated lens-on-sphere structure, or to revert to a well-mixed alcohol rich phase.[41]

The paper is organized as follows. In Section II, we briefly review the potential effects *n*-alcohols can have on water freezing and use established models to estimate the surface enrichment of alcohol in nanodroplets. Section III describes the experimental and data analysis methods. Section IV contains a summary and discussion the results, leading to the conclusions described in Section V.

II. Freezing of aqueous-alcohol solutions and aerosol surface partitioning

Pure water has an equilibrium melting/freezing point of 273.15 K at atmospheric pressure. In an ideal aqueous solution, for which the solute–water and water–water interactions are indistinguishable, the equilibrium freezing temperature is lower than that of the pure solvent in keeping with the corresponding colligative properties. Water, however, can be supercooled significantly before freezing occurs, and for micron sized droplets the limit of homogeneous ice nucleation T_h is $\sim$235 K at 1 atmosphere.[42] For aqueous-alcohol solutions T_h further decreases, in keeping with the corresponding decrease in water activity.[24] At high solute concentrations, glass formation, rather than ice nucleation may occur even at moderate cooling rates. The vitrification temperature T_g, in turn, depends on molar mass and hydrophobicity of the solute species, and increases as the solution becomes more concentrated.[24] Finally, experiments also show that for the water–1-propanol system, when the propanol mole fraction $x_{propanol} < 0.078$, pure ice forms as the mixture is cooled below the equilibrium melting temperature, and is in equilibrium with a solution enriched in 1-propanol.[43] However, as the temperature drops below the peritectic point $\sim$263.05 K, the two phases in equilibrium are the water ice and propanol clathrate hydrate.[43] Thus, even the relatively simple aqueous-alcohol systems are expected to exhibit a rich range of freezing and phase-separation behaviors as the droplets cool.

The larger surface-to-volume ratio of multicomponent aerosol nanodroplets is also expected to lead to different surface partitioning behavior than the corresponding macroscopic solutions. Thus, one expects the changes in freezing temperature and freezing rate in nanodroplets to differ from those in a macroscopic solution and to depend strongly on the amphiphilic solute.

There are a number of models available to estimate the partitioning between the surface and the interior. These include models based on the Gibbs adsorption isotherm,[30,44] the monolayer model where the organic compound is assumed to only aggregate in the surface phase, and the compressed film model where surface tension is related to the surface coverage.[45] Here we present a more-detailed description of predictions obtained using the model proposed by Malila and Prisle.[46] In this model, a spherical droplet of radius r is treated as if it were composed of two phases with different compositions and properties: the interior or bulk (superscript b) and a surface monolayer (superscript s) that covers the core. The distribution of the surface active species between the bulk and the surface is determined by equating the surface tension of the droplet, as determined by the interior mole fraction x^b, with the volume fraction weighted surface tensions of the pure components in the surface layer, *i.e.*

$$\sigma(x^b, T) = \frac{\sigma_1 v_1 x_1^s + \sigma_2 v_2 x_2^s}{v_1 x_1^s + v_2 x_2^s}. \quad (1)$$

Here, the subscripts 1 and 2 refer to water and the alcohol, respectively and v_i represents the molecular volume of species i. Eqn (1) may be solved iteratively and must also satisfy the mass balance constraints imposed by the size and overall composition of the droplet. A more detailed description of this model, as well as the data used to fit $\sigma(x^b,T)$, at the temperatures of interest, is provided in the ESI† (Sections S.I and S.V, respectively).

Fig. 1 shows the resulting surface partitioning predictions for droplets of r = 6 nm, plotted as a function of the overall droplet composition. The calculated bulk mole fraction of pentanol when the overall composition $x_{pentanol}$ = 0.061 (x_2^b = 0.0029) is still well below the solubility limit of the water-rich phase at 298 K[37] (x_2^b = 0.0044). Furthermore, as detailed in the ESI† (Section S.V.B, Fig. S13), the solubility of 1-pentanol increases as temperature decreases and there may be a lower critical solution temperature below $\sim$200 K. Hence, it is safe to assume that at the 1-pentanol concentrations used in this study there is no additional liquid–liquid phase separation within the droplet beyond surface partitioning. Based on the diffusivity of alcohol in aqueous-alcohol mixtures (Section S.III.C, ESI†), we also estimated that the time required for the droplet structure to equilibrate is in the order of $\sim$1 μs. This timescale is comparable to that found in MD simulations of aqueous-butanol nanodroplets (r = 3 nm, T = 250 K) where stable droplet structures were established well within the 100 ns simulation time whether the initial droplet structure was well-mixed or core–shell.[41]

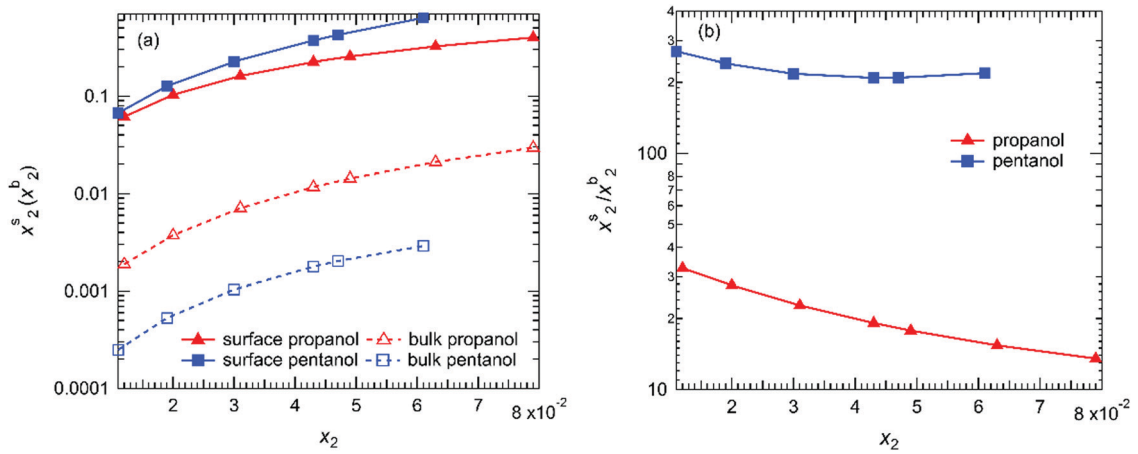

Fig. 1 (a) Mole fraction of alcohols in the surface (x_2^s) and bulk (x_2^b) calculated with the Malila and Prisle[46] model at 220 K for droplets with r = 6 nm. (b) The surface enrichment factor x_2^s/x_2^b at 220 K. Varying the droplet radius by ±0.5 nm, changes the surface enrichment factor by less than ±4% for both alcohols and these changes are well within the symbol size.

Both the surface phase mole fraction x_2^s and the surface enrichment factors x_2^s/x_2^b for 1-propanol and 1-pentanol are consistent with the fact that interfacial adsorption is more favorable for pentanol than propanol due to its longer alkyl chain. The trends for x_2^s/x_2^b, shown in Fig. 1(b), agree with the X-ray photoelectron spectroscopy (XPS) measurements on bulk C4–C6 aqueous-alcohol mixtures at low alcohol concentrations.[47] In particular, for 1-pentanol at T = 283 K and x_2^b = 0.003 (solubility limit is ~0.005 at T = 283 K),[37] Walz *et al.*[47] reported a maximum surface enrichment of ~130, a value that is somewhat lower than that predicted here but still of the same order of magnitude.

The more rapid levelling-off of x_2^s/x_2^b for 1-pentanol also reflects the more rapid decrease in surface tension for 1-pentanol relative to 1-propanol at comparable mole fractions. The simulations reported by Ballal and Chapman[34] also showed that interfacial tensions decrease more drastically and level off earlier for aqueous solutions of alcohols with longer chain lengths.

Given the low concentrations of 1-pentanol in the droplet interior, an alternate approach of calculating surface-bulk partitioning in the partially miscible aqueous-pentanol droplets, is to assume that all 1-pentanol molecules reside at the air–water interface and only dissolve in the interior after the surface becomes saturated. If one assumes that a 1-pentanol molecule occupies[48] 32 Å^2 and that r = 6 nm, full occupancy of the droplet surface corresponds to an overall pentanol concentration of x_2 ~ 0.046.

The Malila and Prisle[46] model, experiments, and simulations, all suggest that 1-pentanol segregates more strongly to the surface than 1-propanol, and, therefore, 1-propanol should affect water freezing more significantly than 1-pentanol at comparable overall molar concentrations.

III. Experiments and methods

A. Flow system and pressure trace measurements (PTM)

All experiments are performed in the supersonic nozzle apparatus illustrated in Fig. 2. The nozzle (nozzle C) has a rectangular cross section with flat sidewalls separated by 1.27 cm, and converging-diverging top and bottom blocks (see Fig. S1 for more details, ESI†). The area of the nozzle throat A^* is 0.635 cm^2 and the effective expansion rate d($A(z)/A^*$)/dz is ~0.086 cm^{-1}, where $A(z)$ is the cross-sectional area z cm downstream of the effective throat (z = 0). This expansion rate leads to cooling rates on the order of 5 × 10^5 K s^{-1}. Each sidewall contains a 14.5 cm long × 1.2 cm high × 3 mm thick CaF_2 window for optical access. As the gas mixture flows through the nozzle, rapid cooling first creates a highly supersaturated vapor phase since the equilibrium vapor pressure $p_{eq,i}$ of the condensable material decreases far more rapidly than its partial pressure p_i. At high enough supersaturation $S = p_i/p_{eq,i}$, the vapor condenses to form nanodroplets, releasing heat to the flow and quenching further particle formation. Once particle growth is complete, the mixed flow again cools as it continues to expand. If low enough temperatures are reached the liquid droplets can freeze.

The carrier gas, N_2, is drawn from the gas side of liquid Dewars ensuring a highly pure, particle free, source. Carrier gas is essential in these experiments because it ensures that the fluid mechanics within the nozzle are accurately described by the supersonic flow equations that incorporate heat addition. The carrier gas does not condense because its partial pressure is always well below the equilibrium vapor pressure even at the lowest temperatures. Nor does it interfere or directly participate in nucleation at these low pressures.[49] Water and alcohol are vaporized separately in the presence of carrier gas, and their flow rates are controlled by two peristaltic pumps and monitored by two balances. The vapor rich stream is mixed into the main carrier gas stream and the combined gas mixture flows continuously into the plenum before it enters the supersonic nozzle. The stagnation pressure is maintained at p_0 = 60.0 kPa, and is determined by measuring the static pressure at a sidewall pressure tap near the nozzle entrance and correcting for the kinetic energy of the flow. The stagnation temperature, maintained at T_0 = 35 °C, is controlled by a water bath and

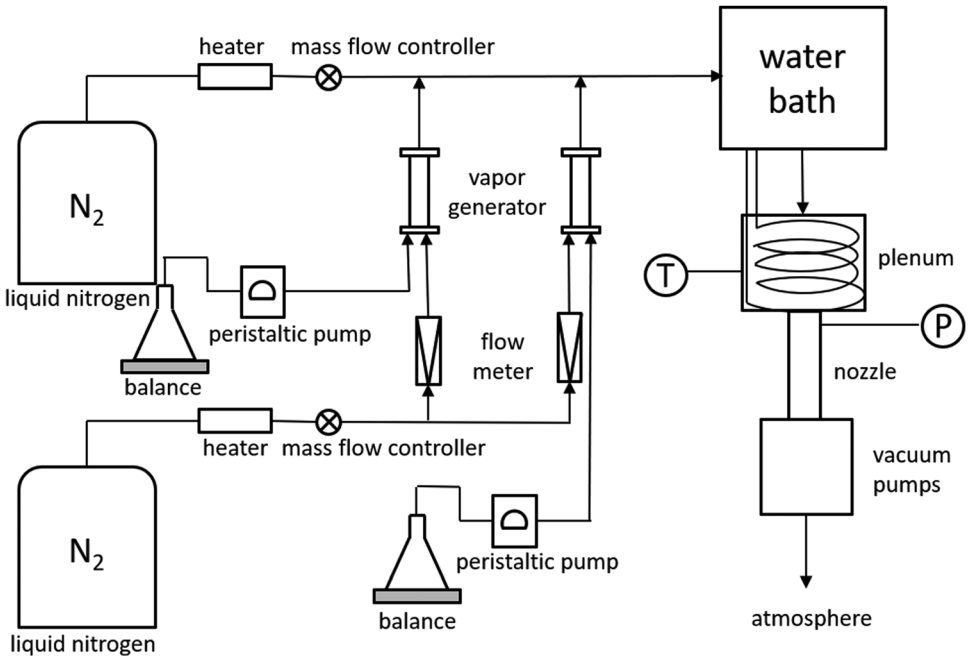

Fig. 2 Schematic of the flow system.

monitored by a platinum resistance temperature detector in the plenum. The water flow rate is fixed to yield an initial mole fraction of water $y_{0,H_2O} = 0.0166 \pm 3 \times 10^{-4}$ with respect to all of entering materials, *i.e.* nitrogen, water, and alcohol, or equivalently to maintain an initial partial pressure $p_{0,H_2O} = 0.99 \pm 0.02$ kPa. The alcohol flow rate is controlled to yield different vapor phase mole fractions, so that the alcohol mole fraction of the total condensate $x_2 = \frac{y_{0,\text{alcohol}}}{y_{0,\text{alcohol}} + y_{0,H_2O}}$ ranges from roughly 0.005 to 0.08. After the flow traverses the nozzle it is exhausted to atmosphere by two rotary vane vacuum pumps.

In a PTM, a movable pressure probe measures the local static along the center line of the nozzle. As noted above, $z = 0$ corresponds to the effective nozzle throat that is $\sim$0.12 cm downstream of the physical throat due to boundary layer development along the nozzle walls. Pressure measurements are taken every 0.1 cm in the subsonic region (-1.0 cm $< z < -0.2$ cm), every 0.04 cm near the throat (-0.2 cm $< z < 0.2$ cm) every 0.1 cm up to $z = 2.6$ cm, and then every 0.2 cm to the end of the nozzle ($z \sim 10.3$ cm). When the mixed vapor condenses in the supersonic portion of the nozzle, the latent heat released by the phase transition leads to a deviation in the static pressure from the expected isentropic expansion. This deviation is detected by comparing the position-resolved static pressure p measured for carrier gas alone (dry trace) with that measured for a condensable-carrier gas mixture (wet trace). The dry trace also characterizes the effective area ratio of the nozzle $A(z)/A^*$. The other variables of the flow, including temperature T, flow velocity u, density ρ, and mass fraction of condensate g, are calculated by solving the compressible flow equations with heat addition using p and $A(z)/A^*$, as the known variables.[50] As part of the integration scheme the raw pressure measurements are interpolated to provide data points every 0.01 cm.

The analysis detailed above assumes $A(z)/A^*$ is not affected by condensation. However, this is not strictly true as the boundary layers that develop along the nozzle walls can be compressed as condensation occurs.[51] Under our experimental conditions, the temperature can be systematically underestimated by about 4 K when boundary layer compression is ignored. To correct for this effect, we therefore use g values determined from an integrated analysis of small angle X-ray scattering and PTM data collected under similar operating conditions and water partial pressures ($p_{0,H2O} = 1.05$ kPa) in the same nozzle.[52] Using the values of g and p as input, the other flow properties – in particular the temperature – can be estimated more accurately. The small angle X-ray scattering experiments also found that the average particle sizes for water–1-pentanol aerosols produced from initial conditions of $p_{0,H2O} = 1.05$ kPa and x_{pentanol} values between 0 and 0.062, had average radii $\langle r \rangle$ ranging from 5.6–7.0 nm (see Fig. S15, ESI†).[52] Thus, we assume that for all the particles in the current study $\langle r \rangle \sim 6$ nm. As noted in Fig. 1, our partitioning analysis is not significantly affected by changing the size from 5.5 nm to 6.5 nm.

B. Fourier transform infrared spectroscopy (FTIR)

FTIR is a powerful approach to interrogate the H-bonding network in water and to follow the liquid–solid phase transition of water *via* changes in the O–H stretch band. Thus, aerosol freezing is probed by observing changes to the position-resolved IR spectra within the O–H stretch region 3000–3600 cm^{-1}. The C–H stretch bands in the 3000–2800 cm^{-1} range contributed by the alcohols are also monitored as a reference.

In our setup the IR beam, guided by two focusing mirrors and one plane mirror, passes through the nozzle and is detected by a liquid nitrogen cooled MCT detector. At each position in the nozzle, 32 spectra are measured with a resolution

of 1 cm^{-1}, no apodization, and with the software suppression of the H_2O/CO_2 vapor lines turned on in order to minimize the contribution of these species in the room air to the final spectra. A spectrum of the carrier gas alone is taken as background at each position before measuring the absorption due to the sample. Since the density of the gas mixture varies as a function of position in the nozzle and the mass fraction of the condensate changes during the vapor to liquid phase transition, the measured absorbance is normalized using

$$\varepsilon_a(\nu) = -\log\left(\frac{I_s(\nu)}{I_e(\nu)}\right) \times \frac{\bar{m}}{l\rho g} \quad (2)$$

where $I_s(\nu)$ denotes the measured intensity of light passing through the mixture (the sample) as a function of the wavenumber ν, $I_e(\nu)$ is the measured intensity of light passing through the carrier gas only (the background), $\bar{m}$ denotes the molecular weight of the condensate, l is the beam path length, *i.e.* the nozzle block width in our case, ρ is the flow density calculated from the PTM, and g is the mass fraction of the condensate. The units of $\varepsilon_a(\nu)$ are m^2 mol^{-1}.

C. SMCR analysis

To further quantify the O–H stretch band of the IR spectra, a self-modelling curve resolution (SMCR) analysis was performed on each set of spectra corresponding to a fixed alcohol mole fraction. The SMCR procedure decomposes a set of spectra into linear combinations of two non-negative, linearly independent underlying component spectra without any constraints on the corresponding spectral shapes.[53,54] One may, however, constrain the shape of one of the SMCR components to match the experimental spectrum of a particular solution, as has previously been done in treating temperature dependent Raman spectra of water as mixtures of high and low temperature spectral components.[55–57] Here we employ a similar strategy to analyze the temperature dependent FTIR spectra of nanodroplets composed of aqueous alcohol solutions. Specifically, in the first round of SMCR, the spectrum at the highest temperature (here ~231 K) is taken as the "high temperature liquid" reference component spectrum (HTL), and a pairwise SMCR analysis is performed with each of the other measured spectra to decompose those spectra into a linear combination of the HTL and the corresponding SMCR low temperature component spectrum. Prior to the onset of freezing, SMCR yields a series of very similar low temperature component spectra, which we refer to as the "low temperature liquid" component (LTL). The amplitude of the LTL component increases with decreasing temperature, but its shape is approximately temperature independent. The fact that a continuous distribution of water structures can be accurately approximated as a linear combination of two components was explained theoretically by Geissler.[58] When droplets start to freeze, however, the shapes of the low temperature component spectra begin to change significantly, signaling the appearance of a new structural component, due to the corresponding solid phase. After completing the initial pairwise analysis, a global estimate of the LTL can be made by a joint analysis of all of the "liquid-like" spectra.

In order to obtain further information regarding the emergence of the solid phase below the pure liquid region, we performed a second round of SMCR on the first round low temperature component spectra. In this second round SMCR analysis, the LTL component spectrum obtained from the global first round SMCR analysis of the liquid-like spectra is used as the reference spectrum, and the new component spectrum obtained from the second round SMCR analysis of the low temperature component spectra is assigned to the emergent frozen species, and is referred to as the "ice component" (IC).

The fractional area of the IC relative to the LTL component at each temperature provides a quantitative measure of the apparent ice fraction of each spectrum, F'_{IC}. Multiplying F'_{IC} from the second round SMCR by the LTL component fraction from the first round SMCR, yields an estimate of the fraction of the IC spectrum in the full spectrum, F_{IC}. Moreover, if we assume that the IR absorption cross section for the ice and liquid are identical, then we may approximately equate F_{IC} with the corresponding mole fraction of ice in the aerosol. However, since the IR cross section water decreases with decreasing hydrogen-bond strength, the latter estimate is expected to represent an upper bound to the true mole fraction of ice.

Finally, to derive the ice nucleation kinetics we first normalize F_{IC} to 1. This normalization is equivalent to assuming that the aerosol is fully frozen at the lowest temperatures. Thus, the time evolution of the normalized F_{IC} can be used to obtain information about ice-nucleation kinetics under the usual assumptions that (1) the normalized F_{IC} is equivalent to the fraction of aerosol droplets that have frozen F_F, (2) that a single nucleation event within a drop initiates freezing, and (3) that freezing of a single droplet occurs much faster than the time required to freeze the entire aerosol.[13,59,60] Here time and position in the nozzle are related by $dt = dx/u$ where u is the local velocity derived from the PTM. For pure water, the ice nucleation rates derived using SMCR analysis are entirely consistent with those determined using our earlier approach.[13]

D. Chemicals

The carrier gas nitrogen is boiled off from liquid nitrogen (purity of 99.998%) purchased from Praxair. The deionized water had a resistivity of ~18 megohm. The 1-propanol and 1-pentanol (purity ≥99%) were purchased from Sigma-Aldrich Corporation and used without further purification. The physical properties of the pure materials and their mixtures are listed in the Physical Properties section in the ESI† (S.V.A and S.V.B, respectively).

E. Experimental conditions

The base experimental condition corresponds to pure water expanding from an initial partial pressure p_{H2O} = 1.01 kPa, p_0 = 60.0 kPa and T_0 = 35 °C. All other experiments matched this initial partial pressure of water and added alcohol so that the mole fraction of alcohol with respect to the total condensable material was between 0.005 and 0.08. In two additional control experiments, extra water was added at mole fractions of 0.012 and 0.056 relative to the base case. Approximately 25 FTIR position resolved measurements were made for the base water case and each aqueous-alcohol experimental condition.

IV. Results and discussion

A. Pressure trace measurements

PTMs provide the position resolved temperature, density, and velocity profiles of the flowing gas mixture, as well the mass fraction of the condensate. The robustness of these techniques has been tested in earlier work,[51] and based on those results, the estimated accuracy of the reported temperature is $\sim\pm2$ K. PTMs are used to characterize the conditions required to initiate condensation in the supersonic nozzle and to determine when particle growth is essentially complete. The flow velocity lets us translate between position and time, and, in the nozzle used here, the time required for the flow to pass from the throat to a point 10 cm further downstream is $\sim$210 μs.

Table 1 summarizes all of the results of PTMs and Fig. 3 illustrates representative temperature and pressure traces for water co-condensing with 1-propanol and water co-condensing with 1-pentanol. In both figures, the position z is with respect

Table 1 Experimental conditions and results of PTM for (a) pure water. (b) Water with 1-propanol. (c) Water with 1-pentanol. $\dot{m}$ is the mass flow rate, x is the mole fraction of the condensable material (excluding carrier gas), y_0 is the initial mole fraction in the vapor phase (including carrier gas), p_0 is the initial partial pressure, T_{min} and p_{min} are the minimum temperature and pressure within the nucleation pulse, S_i is the supersaturation of the vapor with respect to the pure liquid at T_{min}. for species i. All expansions started from p_0 = 60.0 kPa and T_0 = 35 °C

$\dot{m}_{H_2O}$ (g min^{-1})	$x_{H_2O}\times100$	$y_{0,H_2O}\times100$	p_{0,H_2O} (kPa)	T_{min} (K)	p_{min,H_2O} (kPa)	S_{H_2O}
(a) Water						
5.52	0	1.69	1.01	219.8	0.28	66
5.66	1.2	1.71	1.02	220.8	0.29	61
5.92	5.6	1.79	1.07	221.5	0.32	61

$\dot{m}_{H_2O}$ (g min^{-1})	$\dot{m}_{PrOH}$ (g min^{-1})	$x_{PrOH}\times100$	$y_{0,H_2O}\times100$	$y_{0,PrOH}\times100$	p_{0,H_2O} (kPa)	$p_{0,PrOH}$ (kPa)	T_{min} (K)	p_{min,H_2O} (kPa)	$p_{min,PrOH}$ (kPa)	S_{H_2O}	S_{PrOH}
(b) Water and 1-propanol											
5.52	0.22	1.2	1.62	0.019	0.97	0.011	221.5	0.28	0.003	54	1.5
5.53	0.38	2.0	1.63	0.034	0.98	0.020	223.1	0.29	0.006	46	2.2
5.51	0.59	3.1	1.63	0.052	0.98	0.032	224.7	0.30	0.010	40	2.9
5.52	0.83	4.3	1.62	0.073	0.98	0.044	226.3	0.30	0.014	34	3.5
5.52	0.96	4.9	1.62	0.084	0.97	0.051	227.1	0.31	0.016	32	3.7
5.51	1.24	6.3	1.61	0.109	0.97	0.065	228.8	0.32	0.022	27	4.0
5.52	1.58	7.9	1.62	0.139	0.97	0.083	230.3	0.33	0.029	24	4.3

$\dot{m}_{H_2O}$ (g min^{-1})	$\dot{m}_{PenOH}$ (g min^{-1})	$x_{PenOH}\times100$	$y_{0,H_2O}\times100$	$y_{0,PenOH}\times100$	p_{0,H_2O} (kPa)	$p_{0,PenOH}$ (kPa)	T_{min} (K)	p_{min,H_2O} (kPa)	$p_{min,PenOH}$ (kPa)	S_{H_2O}	S_{PenOH}
(c) Water and 1-pentanol											
5.52	0.14	0.5	1.69	0.009	1.01	0.005	221.4	0.30	0.002	59	23
5.51	0.29	1.1	1.68	0.018	1.01	0.011	223.8	0.31	0.003	45	34
5.51	0.53	1.9	1.68	0.033	1.01	0.020	226.9	0.32	0.006	34	41
5.51	0.84	3.0	1.66	0.052	1.00	0.031	230.8	0.33	0.010	23	38
5.51	1.20	4.3	1.65	0.073	0.99	0.044	235.2	0.35	0.016	15	31
5.51	1.34	4.7	1.69	0.084	1.01	0.050	235.7	0.37	0.019	15	35
5.57	1.77	6.1	1.67	0.108	1.00	0.065	239.5	0.37	0.024	10	28

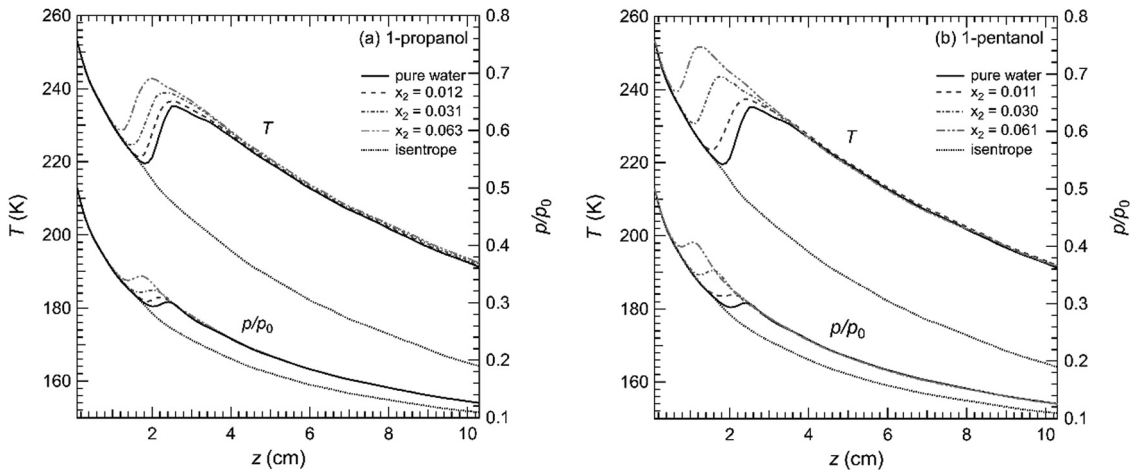

Fig. 3 (a) Pressure and temperature profiles for H_2O with 1-propanol and (b) 1-pentanol at the indicated overall mole fractions of alcohol (x_2). Condensation occurs further upstream as the alcohol concentration increases, and the change is more rapid for 1-pentanol than 1-propanol. All temperatures have been corrected for boundary layer compression associated with condensation.

to the effective throat, and the base case (solid curve) that condenses at the lowest pressure and temperature, corresponds to that of pure water. The other curves are labeled with the mole fraction of alcohol x_2 used in the experiment. In all cases the condensing flow curve closely follows the curve predicted for an isentropic expansion of the same gas mixture (dotted curve labeled isentrope) until the abrupt increase in pressure and temperature indicates the onset of condensation. Here we characterized that onset by the minimum temperature T_{min} reached by the flow in the nucleation zone, since at T_{min} both supersaturation and nucleation rates should be maximized. For the pure water base case, T_{min} corresponds to $\sim$220 K and occurs $\sim$2 cm downstream of the effective throat. Once condensation is complete, the temperature begins to decrease again. Downstream of condensation, the pressure traces do not show any obvious bumps corresponding to freezing because little heat is released when ice crystallizes from supercooled water. The pressure traces corresponding to the remaining conditions are available in Fig. S2 (ESI†).

When extra water is added to the system at comparable molar amounts (Fig. S2, ESI†), condensation only moves upstream by $\sim$0.1 cm due to the slight increase in supersaturation. In contrast, the onset of condensation moves upstream rapidly and occurs at increasingly higher temperatures when equivalent moles of propanol or pentanol are added. The changes in T_{min} with composition indicate that vapor phase nucleation occurs more readily for the water–alcohol mixtures than for pure water. It is well established that in aqueous-alcohol systems, nucleation at a fixed rate occurs at lower activities than expected based on a linear interpolation between the activities required to nucleate the pure components, leading to the conclusion that there is mutual enhancement in the nucleation process for these species.[35,50,61] The mutual enhancement is consistent with a rapid decrease in the free energy required to form new clusters as the presence of alcohol in the clusters decreases the interfacial free energy. These ideas are supported by simulations of vapor–liquid nucleation in the short-chain alcohol–water system by Nellas *et al.* that found significant enrichment of alcohol at low alcohol activity on the cluster surface.[62] The more rapid decrease in surface tension when adding a normal alcohol with longer chain length, as proposed by simulations,[33] and the relative vapor pressures of water, 1-propanol and 1-pentanol (Fig. S10, ESI†), are consistent with our results that at equal vapor phase partial pressures it is easier for water and pentanol to co-condense at higher temperature than for water and propanol to do so. Since the alcohol comprises only a few mole percent of the total condensable flow, and water is the major source of the released heat, the temperature after the burst of particle formation does not change significantly between the different experiments. Although it may not be strictly true, we assume the condensate always has the same composition as the condensable in the initial vapor mixture. As detailed in Section S.III.B (ESI†), this assumption is however quite consistent with the expected vapor pressures of water and alcohol above a 6 nm droplet at the temperature and pressure in the flow near the onset of freezing.

B. Fourier transform infrared spectroscopy: trends and basic interpretation

Fig. 4 summarizes the normalized FTIR spectra for the base case water experiments. Strictly speaking, the temperatures reported in the legend are those of the flow. As reported in our earlier work,[63,64] however, once condensation slows the temperature of the droplets is very close to the flow temperature. As droplets freeze they also heat up very briefly, but as outlined in Section S.III.D (ESI†) the stochastic nature of the freezing process and the time required to freeze the entire aerosol ensures that the average temperature of the aerosol is still within the stated temperature uncertainty. As illustrated in Fig. 4(a), at higher temperatures, the broad shape of the liquid phase droplets reflects the dipole interactions and couplings of different OH bonds.[65] As the temperature decreases the O–H stretch band narrows, the peak intensity increases, and the entire spectrum red shifts, suggesting an increasingly ordered structure. After freezing starts, at $\sim$219 K, the spectra exhibit rapid changes in shape down to $\sim$205 K. Below this temperature the band retains basically the same shape and the slight changes

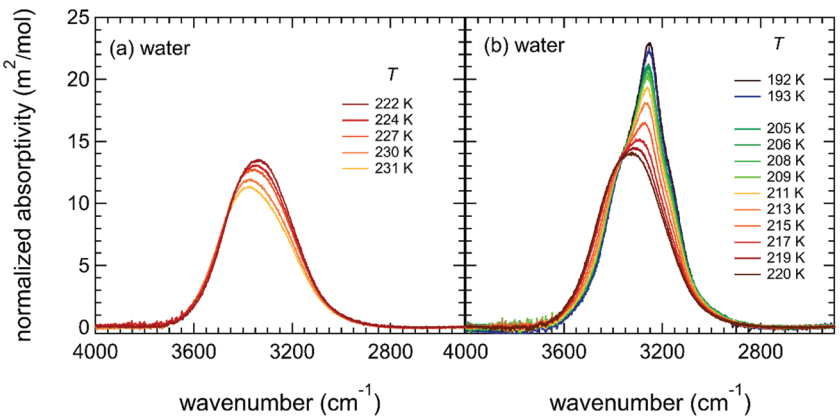

Fig. 4 FTIR spectra for $\langle r \rangle \sim 6$ nm aerosol droplets (particles) of pure water. (a) Liquid water droplets. (b) During the transition from liquid water to ice, the peak shifts to lower wavenumber as temperature decreases. The coldest liquid water spectrum ($\sim$220 K) appears quite symmetric, and spectra become increasingly asymmetric as the aerosol freezes. For clarity, not all spectra measured are illustrated here.

in peak intensity and location are consistent with further cooling of the crystals. When the aerosol is completely frozen, the spectral peak lies near 3250 cm^{-1}, in good agreement with both with the results of Manka *et al.*,[9] Medcraft *et al.*[66] and those of Amaya and Wyslouzil.[13]

For the 1-alcohol experiments, all of the measured spectra not presented in the main text are available in Fig. S3 and S4 of the ESI† whereas Fig. S5 and S6 (ESI†) summarize the changes in peak intensity and position with temperature for all the data. Only selected cases that illustrate the breadth of the data collected are discussed in detail here. In particular, Fig. 5 and 6 present spectra corresponding to alcohol mole fractions $x_2 \sim 0.02$ and ~ 0.06, where the liquid spectra (a & c) have been separated from those for which we observe a transition to a frozen state (b & d). For $x_2 \sim 0.02$, both the liquid and frozen spectra for the two alcohols are very similar in appearance to the pure water spectra, with a slight decrease in the peak intensities, but very similar band shapes. We attribute this behavior to strong partitioning of the alcohols to the surface of the droplets. The low concentration of alcohol within the droplet interior – estimated as $x_2^b = 0.004$ for 1-propanol and $x_2^b = 0.0005$ for 1-pentanol (see Section II) when $x_2 \sim 0.02$ – appears to have little influence on the freezing of the bulk phase. Even if we take into account the relative size of the alcohol and water molecules, the estimated bulk mole fractions correspond to bulk volume fractions of only 0.014 and 0.003, for 1-propanol and 1-pentanol, respectively.

In contrast, the spectra measured for aqueous-alcohol nanodroplets with $x_2 \sim 0.06$ are distinctly different from those for pure water even at temperatures for which pure water or composite droplets at low alcohol concentrations freeze. There is a strong decrease in peak intensities, a blue shift in peak positions and a broadening of the O–H stretch band relative to the coldest frozen spectrum of pure water. Furthermore, while in pure water the band position and intensity change rapidly within a ~ 15 K temperature range as ice nucleation proceeds, for aqueous-alcohol solutions with $x_2 = 0.06$, the transformation of the spectra is much less obvious over a comparable decrease in temperature. This indicates at best a much slower phase transition rate in the presence of the alcohols. At worst, it is not clear that these samples ever form crystalline ice. The changes of the low temperature spectra at high alcohol concentration suggest that the solvated alcohol molecules interrupt the tetrahedral hydrogen bonding network of ice in the interior of the droplet and the structure of solid aqueous-alcohol particles is less ordered than that of pure water ice. This structural disruption is consistent with the fact that while water favors forming 4 H-bonds with two donors and two acceptors, an alcohol molecule can only form up to 3 such H-bonds with one donor and up to two acceptors.

All the mixed droplets also contain features near 2800 cm^{-1} that correspond to the C–H stretch bands. At equal mole fraction, those for 1-pentanol are more intense than those for 1-propanol, in line with the increase in alkyl chain length. Fig. 7 compares the C–H peaks observed for the pure vapor, pure liquid nanodroplets, and the aqueous alcohol nanodroplets at $x_2 \cong 0.06$. For the water–1-propanol nanodroplets, the methyl and methylene peaks are blue shifted by ~ 5–7 cm^{-1} relative to those of pure propanol liquid and are more in line with those of vapor phase propanol. Max *et al.*[67] attributed a similar shift in

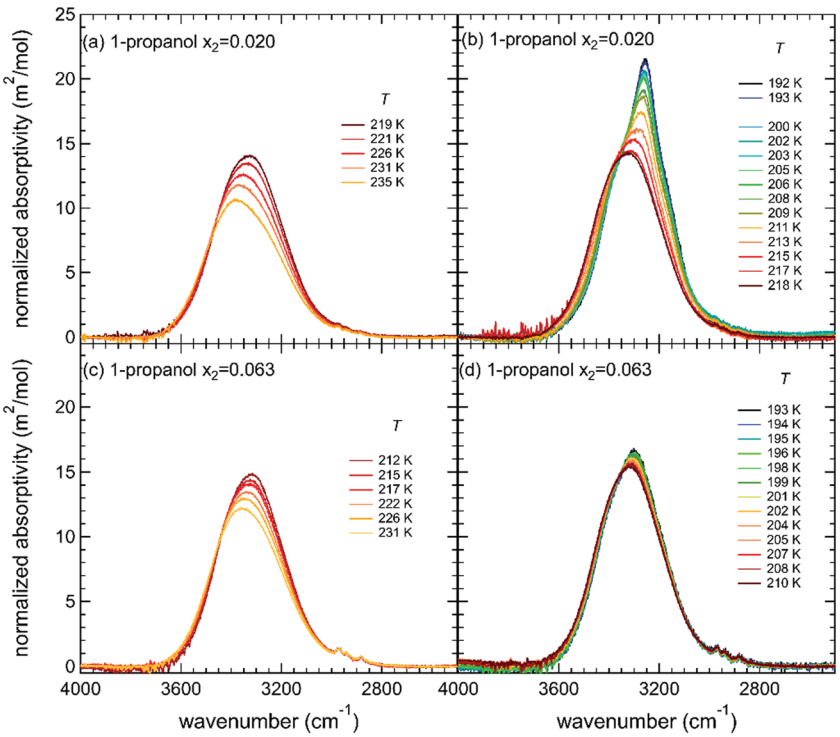

Fig. 5 FTIR spectra for $\langle r \rangle \sim 6$ nm aqueous 1-propanol aerosol droplets (particles). (a and b) $x_2 = 0.020$ (c and d) $x_2 = 0.063$.

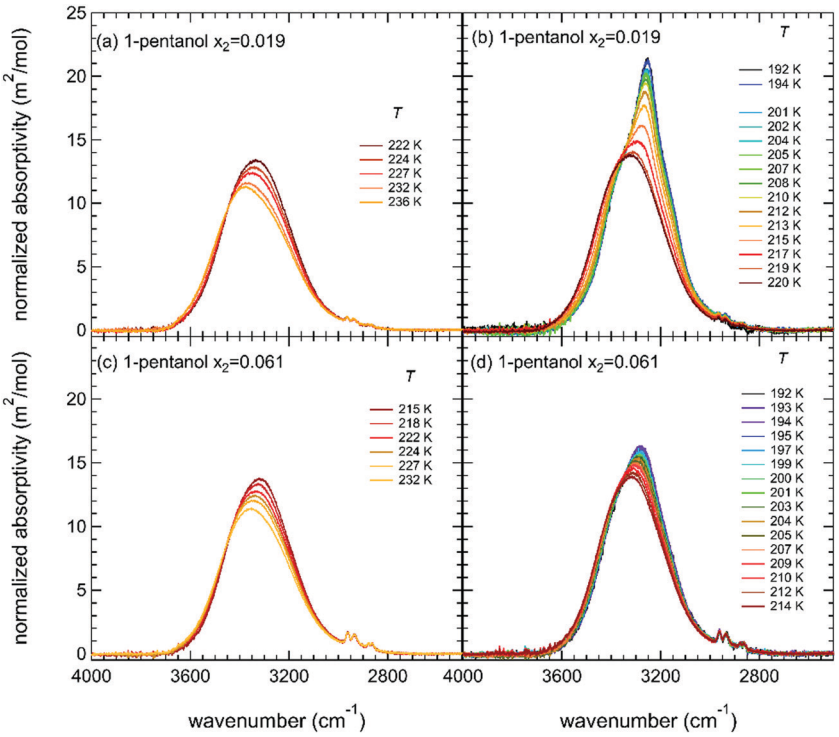

Fig. 6 FTIR spectra for $\langle r \rangle \sim 6$ nm aqueous 1-pentanol aerosol droplets (particles) (a and b) $x_2 = 0.019$ (c and d) $x_2 = 0.061$.

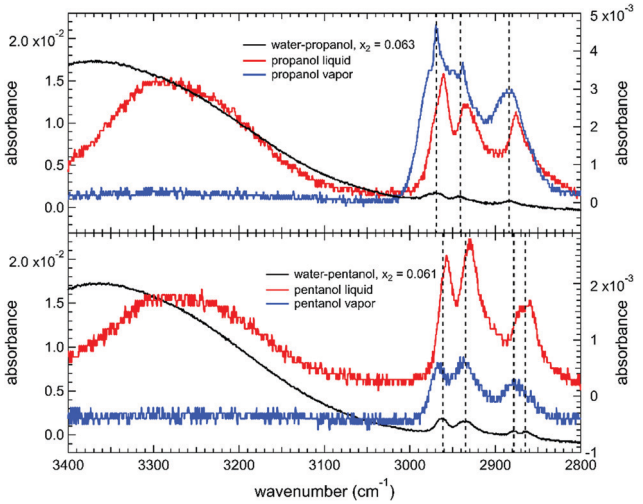

Fig. 7 Spectra for aqueous-alcohol droplets with $x_2 \sim 0.06$ (black, left axis), pure liquid alcohol (red, right axis) and vapor alcohol (blue, right axis). Dashed vertical black lines indicate the peak positions for the C–H stretch in the aqueous-alcohol nanodroplets. Note that the scales on the left and right axes differ.

the peaks of the C–H stretch bands observed in bulk 1-propanol–water mixtures, to the formation of 1-propanol hydrate. Thus, the spectra suggest that the 1-propanol molecules in the mixed droplets are more likely to be isolated or interacting with water molecules, rather than interacting with other propanol molecules. In contrast, for the 1-pentanol–water nanodroplets, the C–H peaks are less shifted from the pure liquid peaks, consistent with the expectation that most of the pentanol molecules reside together on the surface, and fewer are isolated or in a hydrated environment.

C. Fourier transform infrared spectroscopy: SMCR analysis

From the discussion of the IR spectra above, it is clear that at high enough concentration alcohol perturbs the development of a highly-ordered ice structure. To determine whether the ice that forms in the presence of alcohol differs from that formed from pure water, and to better quantify how the kinetics of ice nucleation may be altered by the alcohols, we apply the SMCR analysis outlined in Section III. Two rounds of SMCR yields the respective LTL and IC for each data set.

C.1 Low temperature liquid water and ice. The O–H stretch band of liquid water is known to be quite temperature sensitive.[55–57] In our SMCR decomposition of the temperature dependent droplet spectra, we take a measured HTL ($T \sim 231$ K) as one of the components, and obtain a LTL component from SMCR decomposition of the lower temperature spectra. The LTL spectra for pure water and selected 1-propanol mole fractions are shown in Fig. 8 together with their respective HTL reference spectra. The LTL component spectra for the other 1-propanol solutions and all of the 1-pentanol experiments are summarized in Fig. S7 (ESI†). All LTL component spectra peak near the same frequency $\sim 3301 \pm 4$ cm^{-1} and have remarkably similar band shapes. The most significant differences are in the C–H stretch regions where new peaks emerge that reflect the changing level of alcohol in the sample.

The IC spectra extracted from two rounds of SMCR analysis are plotted in Fig. 9. For pure water, 0.012–0.031 1-propanol and 0.011–0.043 1-pentanol, the IC spectra all have essentially

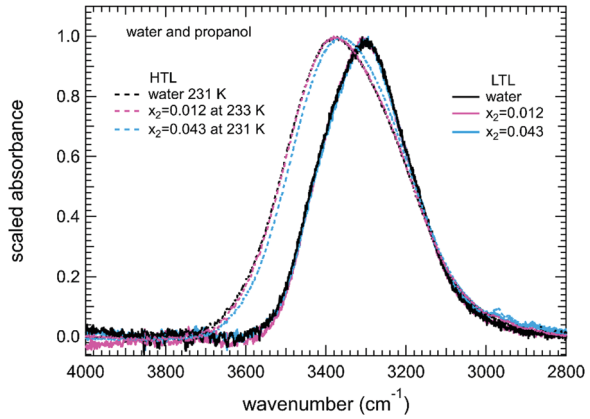

Fig. 8 HTL reference and LTL component spectra from the first round SMCR analysis for water and aqueous propanol solutions with two different concentrations. The temperature corresponding to the HTL is noted in the figure and is ~231 K. All peak intensities are arbitrarily scaled to 1 for easy comparison of the shape of the spectra.

the same shape, thus implying that they all pertain to the formation of ice particles of the same composition. Fig. S8 (ESI†) confirms that two independent analyses using different choices for the temperature range yield essentially the same IC spectra. Furthermore, Fig. S9 (ESI†) confirms that the either analysis yields very similar F_{IC} *versus* temperature curves. The IC band peak at ~3250 cm^{-1} is consistent with the O–H stretch band peak position of ice nanoparticles at 205 K reported by Medcraft *et al.*[66] and the earlier results of Manka *et al.*[9] and Amaya and Wyslouzil.[13] Although the peak position for ice is sensitive to temperature, particle size and experimental set up, Medcraft *et al.* reported that for particles with radii between 4 and ~100 nm, it is largely size independent. Thus, the lower O–H peak ~3220 cm^{-1} reported by Devlin *et al.* for 12 nm diameter particles reflects the much lower temperature (5 K) in their experiments.[65] The fact that the IC spectra derived from different data sets measured here agree so well, suggests that ice formed in the aqueous alcohol nanodroplets is composed of essentially pure H_2O ice, up to overall alcohol mole fractions of 0.031 for propanol or 0.043 for pentanol. As the alcohol concentrations increase further, however, the IC peaks shift to higher frequencies and the spectra broaden. This suggests that at high alcohol concentration, above that at which the surface becomes saturated with alcohol (estimated earlier as $x_2 > \sim 0.046$), the solid that is formed is no longer identical to pure H_2O ice, but rather has a structure that is disordered by the presence of alcohol molecules. Note that this disorder could be due to the incorporation of alcohol into the solid crystal or perhaps to alcohol-induced vitrification to form a glassy H_2O solid that may (or may not) contain alcohol molecules. The broader IC spectrum observed for 1-propanol at comparable overall 1-pentanol concentrations, suggests that propanol perturbs ice freezing more drastically than pentanol, despite its shorter chain length. This result is likely linked to the higher solubility of 1-propanol, in keeping with the partitioning calculations in Section II, which indicate that the bulk concentration of propanol should be almost an order of magnitude higher than that of pentanol for the same overall mole fraction.

For pure water, Fig. 10 illustrates how well the measured and reconstructed spectra agree for a partially frozen aerosol at 205 K. The relative contributions from the HTL reference spectrum, the LTL component and the IC spectrum are also shown. The question remains whether any ice is forming within the particles at higher alcohol concentrations or not? In an effort to address this question, we first tried to fit all of the intermediate spectra where alcohol is present (*i.e.* those spectra between the onset and completion of ice nucleation from which the HTL component has been removed) to a linear combination of the LTL and the IC spectra for pure water. As illustrated in Fig. 11, for $x_{pentanol}$ = 0.030, this approach works well. Furthermore, as shown in Fig. 12, for the intermediate spectra the apparent fraction of the IC F'_{IC} derived this way is very close to that derived directly from the SMCR analysis. This is not surprising given the good agreement between both the LTL and IC spectra derived from SMCR at lower alcohol concentrations.

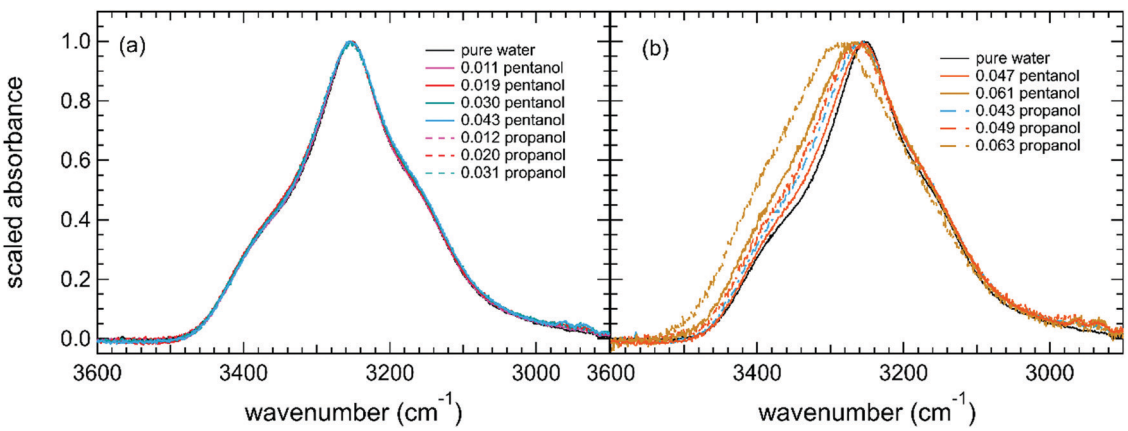

Fig. 9 IC spectra derived from the second round SMCR analysis. (a) For pure water, $0.012 \leq x_{propanol} \leq 0.031$ and $0.011 \leq x_{pentanol} \leq 0.043$; (b) for pure water, $x_{propanol} \geq 0.043$, and $x_{pentanol} \geq 0.047$.

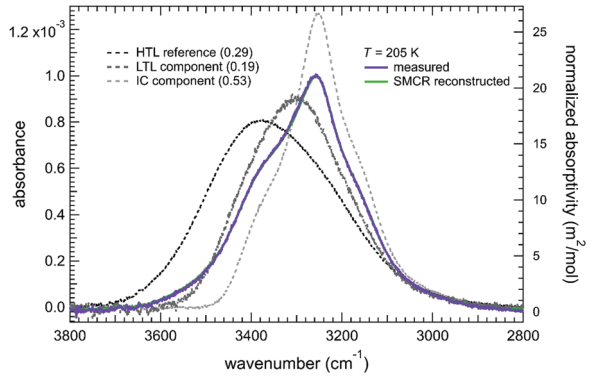

Fig. 10 The normalized spectrum measured for pure water at 205 K (purple, right axis) is well described by a linear combination (green) of the HTL reference, the LTL, and the IC spectra (left axis), with the fraction of each component included in parenthesis.

For the higher alcohol concentrations (*e.g.* 0.063 mole fraction of propanol), however, the measured spectra are no longer satisfactorily fit to a linear combination of the pure water LTL and IC spectra, as there are significant deviations between the least squares best fit and the actual spectra (Fig. 11b). The poorer fitting – despite a low temperature liquid component that is very close to that for pure water – suggests that the end state is no longer highly-ordered ice. The final state may be closer to an amorphous or glassy one due to perturbations to the water network caused by the alcohol molecules within the interior. Alternatively, if ice is forming, the remaining liquid will be enriched in the alcohol and may, therefore, differ enough from pure water's LTL that the spectra cannot be fit by these two components alone. In the absence of other characterization methods, in particular wide angle X-ray scattering,[60] it is not possible to state definitively whether crystalline ice domains form at the highest alcohol concentrations. Despite these uncertainties, when we apply the pure water spectral fitting procedure to the high alcohol concentration data we find that

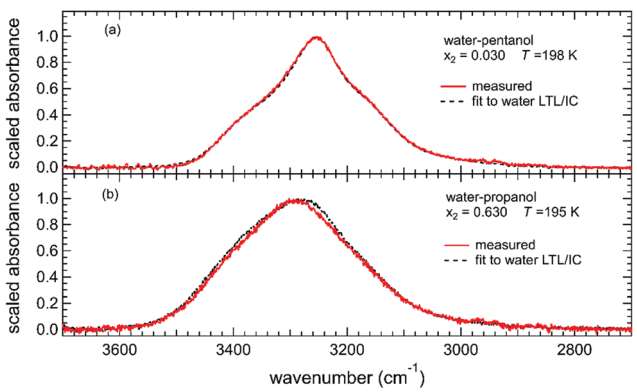

Fig. 11 The low temperature aqueous-alcohol component spectra derived from the first round SMCR analysis (red curve) are fit to a linear combination of the LTL and IC for pure water (black). (a) The fit to the 1-pentanol data at x_2 = 0.03 is very good. (b) For 1-propanol at x_2 = 0.063, neither the band shape nor the peak position are well fit using this approach.

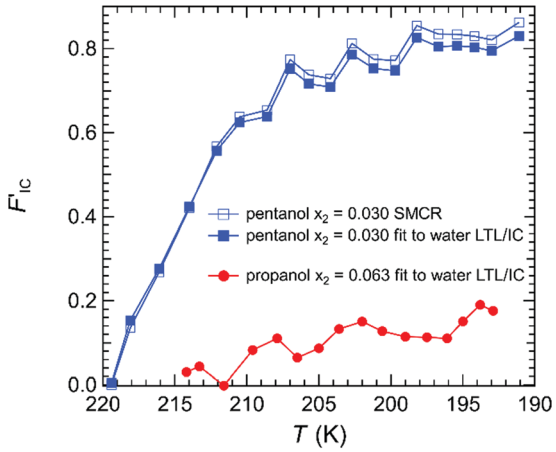

Fig. 12 The apparent ice fraction F'_{IC} (IC fraction of spectrum after HTL component has been removed) is shown as a function of temperature. The pentanol results correspond to (1) direct SMCR analysis of the aqueous-alcohol data (open squares), or (2) fits of the intermediate spectra to a linear combination of the LTL and IC derived from SMCR for pure water (filled squares). The $x_{propanol}$ = 0.063 data were fit using the LTL and IC derived from SMCR for pure water (filled circles).

for $x_{propanol}$ = 0.063 the apparent ice fraction approaches ~20% at the nozzle exit. MD simulations of aqueous-alcohol nandroplet freezing could perhaps help to elucidate the structure of the solid formed in such concentrated aqueous alcohol solutions.

Finally, in Fig. 13 we compare the spectrum for our $\langle r \rangle \sim$ 6 nm ice particles at 192 K to measurements made by Medcraft *et al.* on $\langle r \rangle >$ 25 nm radius particles at about the same temperature.[66] The spectra overlap on the low frequency side but the spectrum for the smaller particles is significantly broader on the high frequency side. Intensity in the high wavenumber portion of the spectrum arises from the disordered surface and the strained subsurface region.[65] In nanoparticles, molecules near the surface make important contributions to the spectrum,

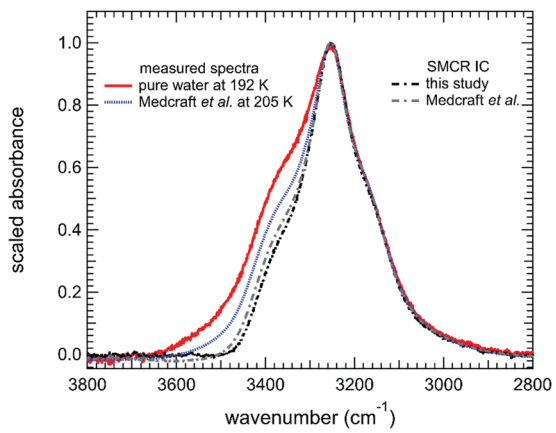

Fig. 13 The IC of pure water (our data: black dash-dotted; Medcraft *et al.* data: grey dash-dotted) derived from the SCMR analysis is distinctly narrower on the high frequency side than the pure water spectrum measured for the $\langle r \rangle \sim$ 6 nm particles (red solid line) at 192 K or the $\langle r \rangle >$ 25 nm particles (blue dotted line) at 205 K measured by Medcraft *et al.* On the low frequency side, the spectra overlap and this is the sign of a crystalline structure in the particles.

especially for particles with $\langle r \rangle \leq 2$ nm, and a simple scaling law suggests the fraction of molecules in the surface phase,[65] is $\sim 0.9/r$ (r in nm). Thus, the spectrum of ice at 205 K for the $\langle r \rangle >$ 25 nm particles[66] with a surface fraction <0.04 should be narrower on the high frequency side than our $\langle r \rangle \sim 6$ nm particles with a surface fraction of ~ 0.15.

The consistency of the two spectra is further confirmed by SMCR. In particular, when we analyze the Medcraft *et al.* spectrum using our HTL and LTL reference spectra, SMCR yields an IC that is extremely close to that derived from our data alone. Furthermore, the large particle spectrum follows the SMCR IC spectrum over most of the wavenumber range, only deviating for wavenumbers above ~ 3300 cm^{-1}. The fact that the SMCR IC spectrum is narrower than the measured ice spectrum is consistent with the fact that the SMCR derived IC is a lower bound for true ice spectrum. In particular it represents the smallest area, non-negative, linearly independent component in the input set of two (or more) spectra. Note that both the LTL and the IC spectra can be described this way. The LTL component is, however, obtained from a two-component decomposition of pairs of low and high temperature liquid spectra, and whereas the IC comes from a two-component decomposition of a LTL spectrum and a spectrum consisting of a mixture of the LTL and ice. Thus, the true ice spectrum may be equivalent to the IC spectrum plus a small amount of the LTL spectrum. Note that such a linear combination is also what would be expected given that the experimental spectra of ice nano-particles should consist of a mixture of bulk crystal and interfacial amorphous or liquid-like components.

C.2 Freezing kinetics. Fig. 14 illustrates the change in the IC fraction, F_{IC}, with temperature for the pure water and low alcohol mole fraction aerosols. The values of F_{IC} in Fig. 14 are lower than the apparent ice fraction values reported in Fig. 12 because the contribution of the HTL is now included. The experiments where the final state of the aerosol is ambiguous ($x_{pentanol}$ = 0.047 and 0.061, $x_{propanol} \geq 0.043$), are excluded from this analysis.

For pure water, ice starts to form at ~ 219 K. As the flow expands and temperature decreases, F_{IC} increases rapidly during an ice nucleation pulse that lasts ~ 40 μs. Once the aerosol is fully frozen, *i.e.* the spectra remain essentially unchanged, F_{IC} plateaus at ~ 0.55. This value is less than 1.0 both because the surface and subsurface phase in our nanoparticles is not fully crystalline, and because the IC spectrum is still narrower than the ice spectrum reported by Medcraft *et al.* for a particle size where surface contributions should be negligible. As $x_{propanol}$ increases from 0.012 to 0.031, the onset of freezing is gradually delayed relative to pure water, but the final F_{IC} still plateaus at values close to those for pure water, suggesting comparable levels of ice formation. In contrast, for $x_{pentanol}$ between 0.011 and 0.030, the change in F_{IC} with temperature (or time) barely differs from the pure water case. A large discrepancy only appears when $x_{pentanol}$ increases from 0.030 to 0.043. As demonstrated in the theoretical calculations, $x_{pentanol}$ = 0.030 corresponds to a bulk mole fraction of 0.001, and, thus, one pentanol molecule in 1000 water molecules does not appear to perturb the freezing process enough to be detected in our IR measurements. The rapid change in the behavior of F_{IC} occurs when $x_{pentanol}$ increases to 0.043, a value that is close to the concentration, $x_{pentanol}$ = 0.046, for which the surface saturation model predicts the surface of a 6 nm radius droplet is fully packed with pentanol. The latter value is expected to be an upper bound because it assumes close packing of the alcohol molecules without vacancies. In summary, the difference in the freezing behavior between the two alcohols clearly reflects both the aqueous solubility and the surface partitioning of these two molecules.

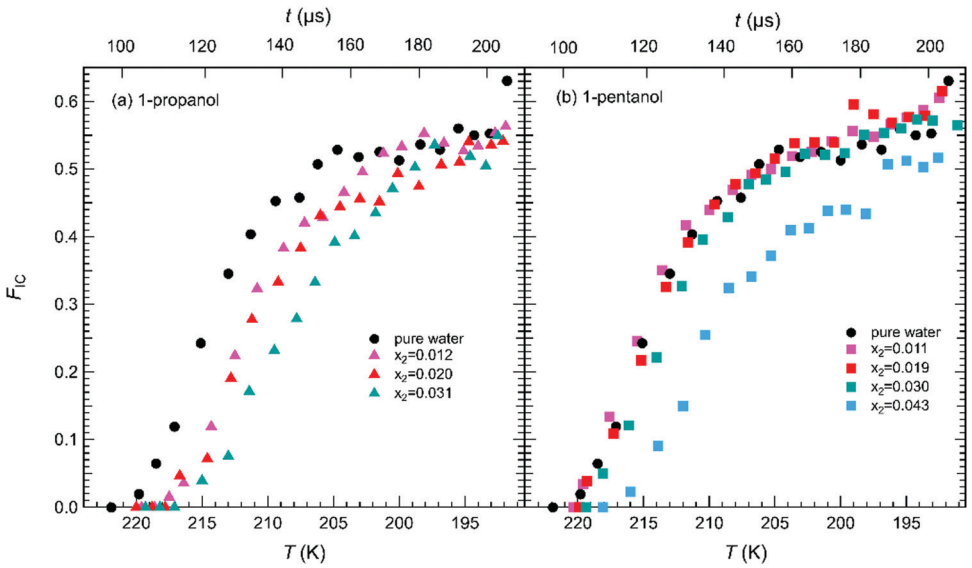

Fig. 14 The change in the IC fraction, F_{IC}, with temperature for (a) pure water and aqueous-propanol aerosols, and (b) pure water and aqueous-pentanol aerosols. The overall alcohol mole fractions are indicated. The top time axis corresponds to the pure water case, but relative times for the alcohol mixtures are very similar.

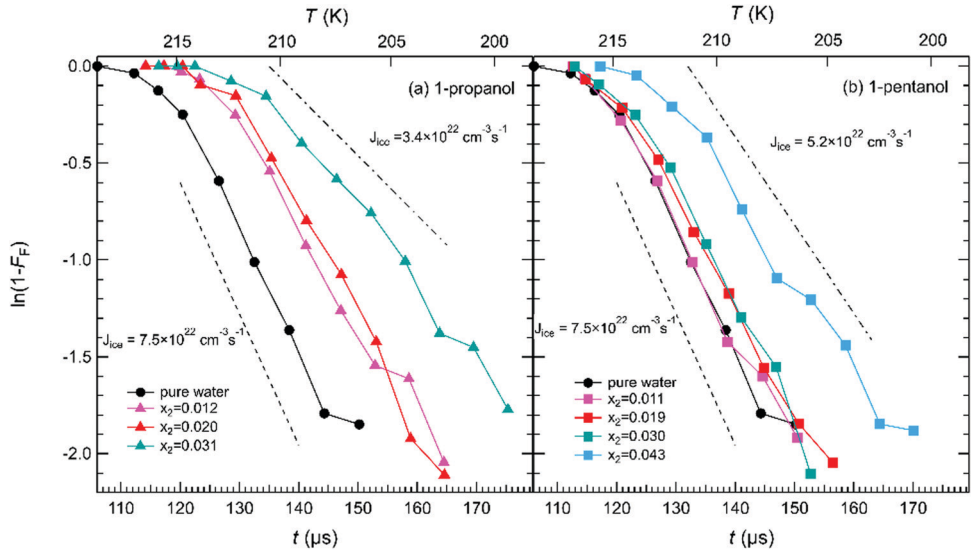

Fig. 15 The slopes of $\ln(1 - F_F)$ *vs.* time curves reflect the ice nucleation rates J_{ice} and the average droplet volume. Time is relative to the effective throat. (a) water with 1-propanol, (b) water with 1-pentanol. The black dashed lines indicate the nucleation rates consistent with the slopes for an average droplet radius of 6 nm. Varying the droplet radius by ±0.5 nm, changes the value of the nucleation rate by less than ±30%.

To extract nucleation rates from the freezing data we start by assuming that if F_{IC} stabilizes by the nozzle exit, the aerosol is fully frozen, *i.e.* the fraction of frozen droplets, $F_F = 1$. Furthermore, we make the usual assumption that when an ice nucleation event occurs within an individual droplet it freezes on a timescale much shorter than the time required to freeze the entire aerosol.[13,59] Thus, normalizing the values of F_{IC} for a data set by its asymptotic value, yields F_F as a function of temperature or time. For the low alcohol data in Fig. 14, whose behavior closely follows that of pure water, these assumptions are reasonable and consistent with previous analysis and simulations. For the high alcohol concentrations, where the ice fraction increases only slowly, these assumptions may no longer hold, *i.e.* the F_{IC} values may reflect a combination of nucleation and ice growth rates.

The ice nucleation rates J_{ice} can be derived from the $F_F(t)$ data *via* the equation[13,59]

$$J_{ice}\langle V\rangle = \frac{1}{t_2 - t_1}\ln\left(\frac{1 - F_F(t_1)}{1 - F_F(t_2)}\right) \quad (3)$$

where $\langle V\rangle$ is the average droplet volume, and t is the travel time of the aerosol relative to the effective throat.

As shown in Fig. 15, the ice nucleation rate is somewhat lower when the ice first appears but rapidly reaches a stable value. For the water-propanol droplets, the onset of ice freezing is delayed as the propanol concentration increases but, as indicated by the essentially parallel slopes, the nucleation rates are all close to the value for pure water, $J_{ice} = 7.5 \times 10^{22}$ cm^{-3} s^{-1}. For the water–pentanol systems, the curves for $x_{pentanol}$ = 0.011–0.030 show only slight deviations from that for pure water. Not only is this consistent with the picture that pentanol resides mostly at the surface where it does not interfere with the ice nucleation process, but the insensitivity to the presence of alcohol also suggests that nucleation is predominately initiated throughout the volume of the droplet not near the surface. For pentanol mole fraction larger than 0.030, the freezing starts later in time (at a lower temperature) and the slope decreases slightly. Finally, for estimated bulk concentrations near 0.002, *i.e.* $x_{pentanol} = 0.043$ ($x_2^b = 0.0018$) and $x_{propanol} = 0.012$ ($x_2^b = 0.0019$), the onset of freezing appears to be delayed by about the same amount but the pentanol droplets may nucleate ice slightly more slowly than the propanol droplets. This result is consistent with pentanol's longer hydrophobic chain length disturbing more water molecules than propanol, as evidenced by hydration shell studies.[54,68]

V. Summary and conclusions

We investigated the freezing behavior of aqueous-alcohol nanodroplets containing mole fractions of 1-propanol or 1-pentanol up to ~0.06. The nanodroplets were produced by condensation in a supersonic nozzle, and both condensation and freezing were characterized by PTM and FTIR spectroscopy. Particle size estimates were available from previous small angle X-ray scattering experiments.[52] At a fixed water concentration and equal molar alcohol concentrations, 1-pentanol was more efficient in initiating particle formation from the vapor phase than 1-propanol. This reflects both the lower vapor pressure of pentanol and the greater decrease in interfacial free energy of cluster formation associated with the higher propensity of pentanol to segregate to the surface.

For pure water and the lower alcohol concentrations ($x_{propanol} \leq 0.031$, $x_{pentanol} \leq 0.043$), changes in the hydrogen-bonded OH stretch region of the IR spectra showed a clear transition from the liquid to a solid state. As the alcohol concentration increased further, there was a reduction in peak intensity and a broadening of the band relative to the pure water spectra. At the highest alcohol concentrations, it was no longer clear whether ice formed.

Two rounds of SMCR analysis were used to decompose the measured spectra into HTL, LTL, and IC spectral components. The LTL spectrum was remarkably consistent across the entire composition range (and to variations in the assumed HTL reference spectrum), and the IC spectrum only changed when $x_{\text{propanol}} \geq 0.043$ or $x_{\text{pentanol}} \geq 0.047$. The consistency of the IC spectra suggests that the ice formed in the aqueous alcohol droplets was the same as that formed in pure water droplets. This finding is consistent with the physical picture that partitioning of the alcohol to the surface of the nanodroplets reduces its ability to hinder freezing. Partitioning calculations suggested that at equal overall molar compositions, surface segregation of the 1-pentanol is much stronger than that of 1-propanol. The resulting higher 1-propanol concentration in the interior of the droplets (at the same overall mole fraction of alcohol) is consistent with our observation that ice nucleation was more significantly perturbed by propanol than pentanol.

The kinetics of ice freezing showed that the presence of propanol delayed the onset of freezing, whereas the onset of freezing was not significantly influenced by 1-pentanol up to $x_{\text{pentanol}} = 0.030$. The systematic decrease in the ice nucleation temperature for propanol and the rapid change when the pentanol concentration increased from 0.030 to 0.043 are consistent with the partitioning preference and solubilities in water of the two alcohols. Remarkably, once ice nucleation was initiated, the rates were not strongly affected, decreasing at most by a factor of 2 for the highest propanol concentration. The relative insensitivity of the nucleation behavior for the low concentration pentanol droplets strongly suggests that nucleation occurs throughout the volume of the nanodroplets rather than at or very near the surface.

Conflicts of interest

There are no conflicts of interest to declare.

Appendix

Table 1 contains a summary of all of the experiments conducted and the results derived from PTM.

Acknowledgements

This work was completed with the financial support of the National Science Foundation under grant numbers CHE-1464924, CHE-1900064 and CHE-1763581. This research used resources of the Advanced Photon Source, a U.S. Department of Energy (DOE) Office of Science User Facility operated for the DOE Office of Science by Argonne National Laboratory under Contract No. DE-AC02-06CH11357.

References

1 B. J. Murray, D. A. Knopf and A. K. Bertram, *Nature*, 2005, **434**, 202–205.
2 M. P. Meyers, P. J. Demott and W. R. Cotton, *J. Appl. Meteorol.*, 1992, **31**, 708–721.
3 R. M. Rasmussen, I. Geresdi, G. Thompson, K. Manning and E. Karplus, *J. Atmos. Sci.*, 2002, **59**, 837–860.
4 A. Tabazadeh, Y. S. Djikaev and H. Reiss, *Proc. Natl. Acad. Sci. U. S. A.*, 2002, **99**, 15873–15878.
5 A. Gettelman, X. Liu, S. J. Ghan, H. Morrison, S. Park, A. J. Conley, S. A. Klein, J. Boyle, D. L. Mitchell and J. L. F. Li, *J. Geophys. Res.: Atmos.*, 2010, **115**, D18216.
6 U. Lohmann and D. Neubauer, *Atmos. Chem. Phys.*, 2018, **18**, 8807–8828.
7 W. Cantrell and A. Heymsfield, *Bull. Am. Meteorol. Soc.*, 2005, **86**, 795–807.
8 B. J. Murray, S. L. Broadley, T. W. Wilson, S. J. Bull, R. H. Wills, H. K. Christenson and E. J. Murray, *Phys. Chem. Chem. Phys.*, 2010, **12**, 10380–10387.
9 A. Manka, H. Pathak, S. Tanimura, J. Wolk, R. Strey and B. E. Wyslouzil, *Phys. Chem. Chem. Phys.*, 2012, **14**, 4505–4516.
10 H. Laksmono, T. A. McQueen, J. A. Sellberg, N. D. Loh, C. Huang, D. Schlesinger, R. G. Sierra, C. Y. Hampton, D. Nordlund, M. Beye, A. V. Martin, A. Barty, M. M. Seibert, M. Messerschmidt, G. J. Williams, S. Boutet, K. Arnann-Winkel, T. Loerting, L. G. M. Pettersson, M. J. Bogan and A. Nilsson, *J. Phys. Chem. Lett.*, 2015, **6**, 2826–2832.
11 T. S. Li, D. Donadio, G. Russo and G. Galli, *Phys. Chem. Chem. Phys.*, 2011, **13**, 19807–19813.
12 A. Haji-Akbari and P. G. Debenedetti, *Proc. Natl. Acad. Sci. U. S. A.*, 2015, **112**, 10582–10588.
13 A. J. Amaya and B. E. Wyslouzil, *J. Chem. Phys.*, 2018, **148**, 084501.
14 D. A. Knopf and Y. J. Rigg, *J. Phys. Chem. A*, 2011, **115**, 762–773.
15 M. M. Conde, M. Rovere and P. Gallo, *J. Mol. Liq.*, 2018, **261**, 513–519.
16 K. Diehl, C. Quick, S. Matthias-Maser, S. K. Mitra and R. Jaenicke, *Atmos. Res.*, 2001, **58**, 75–87.
17 M. Polen, E. Lawlis and R. C. Sullivan, *J. Geophys. Res.: Atmos.*, 2016, **121**, 11666–11678.
18 K. Dreischmeier, C. Budke, L. Wiehemeier, T. Kottke and T. Koop, *Sci. Rep.*, 2017, **7**, 1–13.
19 M. Gavish, R. Popovitzbiro, M. Lahav and L. Leiserowitz, *Science*, 1990, **250**, 973–975.
20 J. Majewski, R. Popovitzbiro, K. Kjaer, J. Alsnielsen, M. Lahav and L. Leiserowitz, *J. Phys. Chem.*, 1994, **98**, 4087–4093.
21 J. Majewski, R. Popovitzbiro, W. G. Bouwman, K. Kjaer, J. Alsnielsen, M. Lahav and L. Leiserowitz, *Chem. – Eur. J.*, 1995, **1**, 304–311.
22 L. H. Seeley and G. T. Seidler, *Phys. Rev. Lett.*, 2001, **87**, 055702.
23 E. Ochshorn and W. Cantrell, *J. Chem. Phys.*, 2006, **124**, 054714.
24 B. Zobrist, C. Marcolli, D. A. Pedernera and T. Koop, *Atmos. Chem. Phys.*, 2008, **8**, 5221–5244.
25 B. J. Murray, *Atmos. Chem. Phys.*, 2008, **8**, 5423–5433.
26 M. J. Kang, P. Q. Fu, S. G. Aggarwal, S. Kumar, Y. Zhao, Y. L. Sun and Z. F. Wang, *Environ. Pollut.*, 2016, **219**, 957–966.

27 G. Isaacman-VanWertz, P. Massoli, R. O'Brien, C. Lim, J. P. Franklin, J. A. Moss, J. F. Hunter, J. B. Nowak, M. R. Canagaratna, P. K. Misztal, C. Arata, J. R. Roscioli, S. T. Herndon, T. B. Onasch, A. T. Lambe, J. T. Jayne, L. P. Su, D. A. Knopf, A. H. Goldstein, D. R. Worsnop and J. H. Kroll, *Nat. Chem.*, 2018, **10**, 462–468.
28 J. D. Felix, J. A. Roebuck, R. N. Mead, J. D. Willey, G. B. Avery and R. J. Kieber, *Atmos. Environ.*, 2019, **217**, 116948.
29 J. D. Willey, G. B. Avery, J. D. Felix, R. J. Kieber, R. N. Mead and M. S. Shimizu, *npj Clim. Atmos. Sci.*, 2019, **2**, 1–5.
30 H. Bianco and A. Marmur, *J. Colloid Interface Sci.*, 1992, **151**, 517–522.
31 A. Laaksonen, *J. Colloid Interface Sci.*, 1993, **159**, 517–519.
32 N. L. Prisle, T. Raatikainen, A. Laaksonen and M. Bilde, *Atmos. Chem. Phys.*, 2010, **10**, 5663–5683.
33 F. Biscay, A. Ghoufi and P. Malfreyt, *J. Chem. Phys.*, 2011, **134**, 044709.
34 D. Ballal and W. G. Chapman, *J. Chem. Phys.*, 2013, **139**, 114706.
35 R. Strey, Y. Viisanen and P. E. Wagner, *J. Chem. Phys.*, 1995, **103**, 4333–4345.
36 B. Chen, J. I. Siepmann and M. L. Klein, *J. Am. Chem. Soc.*, 2003, **125**, 3113–3118.
37 M. Goral, B. Wisniewska-Goclowska and A. Maczynski, *J. Phys. Chem. Ref. Data*, 2006, **35**, 1391–1414.
38 M. Oguni and C. A. Angell, *J. Phys. Chem.*, 1983, **87**, 1848–1851.
39 K. Miyata and H. Kanno, *J. Mol. Liq.*, 2005, **119**, 189–193.
40 B. E. Wyslouzil, G. Wilemski, R. Strey, C. H. Heath and U. Dieregsweiler, *Phys. Chem. Chem. Phys.*, 2006, **8**, 54–57.
41 F. Hrahsheh, Y. S. Wudil and G. Wilemski, *Phys. Chem. Chem. Phys.*, 2017, **19**, 26839–26845.
42 T. Koop, B. P. Luo, A. Tsias and T. Peter, *Nature*, 2000, **406**, 611–614.
43 A. Chapoy, R. Anderson, H. Haghighi, T. Edwards and B. Tohidi, *Ind. Eng. Chem. Res.*, 2008, **47**, 1689–1694.
44 Z. D. Li, A. L. Williams and M. J. Rood, *J. Atmos. Sci.*, 1998, **55**, 1859–1866.
45 C. R. Ruehl, J. F. Davies and K. R. Wilson, *Science*, 2016, **351**, 1447–1450.
46 J. Malila and N. L. Prisle, *J. Adv. Model. Earth Syst.*, 2018, **10**, 3233–3251.
47 M. M. Walz, J. Werner, V. Ekholm, N. L. Prisle, G. Ohrwall and O. Bjorneholm, *Phys. Chem. Chem. Phys.*, 2016, **18**, 6648–6656.
48 M. M. Walz, C. Caleman, J. Werner, V. Ekholm, D. Lundberg, N. L. Prisle, G. Ohrwall and O. Bjorneholm, *Phys. Chem. Chem. Phys.*, 2015, **17**, 14036–14044.
49 M. M. Campagna, J. Hruby, M. E. H. van Dongen and D. M. J. Smeulders, *J. Chem. Phys.*, 2020, **153**, 164303.
50 B. E. Wyslouzil, C. H. Heath, J. L. Cheung and G. Wilemski, *J. Chem. Phys.*, 2000, **113**, 7317–7329.
51 S. Tanimura, Y. Zvinevich, B. E. Wyslouzil, M. Zahniser, J. Shorter, D. Nelson and B. McManus, *J. Chem. Phys.*, 2005, **122**, 194304.
52 A. J. Amaya, PhD thesis, The Ohio State University, 2018.
53 W. H. Lawton and E. A. Sylvestre, *Technometrics*, 1971, **13**, 617–633.
54 J. G. Davis, K. P. Gierszal, P. Wang and D. Ben-Amotz, *Nature*, 2012, **491**, 582–585.
55 S. R. Pattenaude, L. M. Streacker and D. Ben-Amotz, *J. Raman Spectrosc.*, 2018, **49**, 1860–1866.
56 T. Morawietz, O. Marsalek, S. R. Pattenaude, L. M. Streacker, D. Ben-Amotz and T. E. Markland, *J. Phys. Chem. Lett.*, 2018, **9**, 851–857.
57 T. Morawietz, A. S. Urbina, P. K. Wise, X. E. Wu, W. J. Lu, D. Ben-Amotz and T. E. Markland, *J. Phys. Chem. Lett.*, 2019, **10**, 6067–6073.
58 P. L. Geissler, *J. Am. Chem. Soc.*, 2005, **127**, 14930–14935.
59 J. F. Huang and L. S. Bartell, *J. Phys. Chem.*, 1995, **99**, 3924–3931.
60 A. J. Amaya, H. Pathak, V. P. Modak, H. Laksmono, N. D. Loh, A. S. Jonas, R. G. Sierra, T. A. McQueen, M. J. Hayes, G. J. Williams, M. Messerschmidt, S. Boutet, M. J. Bogan, A. Nilsson, C. A. Stan and B. E. Wyslouzil, *J. Phys. Chem. Lett.*, 2017, **8**, 3216–3222.
61 S. Tanimura, H. Pathak and B. E. Wyslouzil, *J. Chem. Phys.*, 2013, **139**, 174311.
62 R. B. Nellas, S. J. Keasler and B. Chen, *J. Phys. Chem. A*, 2008, **112**, 2930–2939.
63 H. Pathak, K. Mullick, S. Tanimura and B. E. Wyslouzil, *Aerosol Sci. Technol.*, 2013, **47**, 1310–1324.
64 Y. Park, S. Tanimura and B. E. Wyslouzil, *Aerosol Sci. Technol.*, 2016, **50**, 773–780.
65 V. Buch, S. Bauerecker, J. P. Devlin, U. Buck and J. K. Kazimirski, *Int. Rev. Phys. Chem.*, 2004, **23**, 375–433.
66 C. Medcraft, D. McNaughton, C. D. Thompson, D. R. T. Appadoo, S. Bauerecker and E. G. Robertson, *Phys. Chem. Chem. Phys.*, 2013, **15**, 3630–3639.
67 J. J. Max, S. Daneault and C. Chapados, *Can. J. Chem.*, 2002, **80**, 113–123.
68 V. Matvejev, M. Zizi and J. Stiens, *J. Phys. Chem. B*, 2012, **116**, 14071–14077.